Delocalized image surface states in defect-free SiO2 hollow nanospheres

J. L. Movilla, F. Rajadell, and J. Planelles[a]

Departament de Química Física i Analítica, UJI, Box 224, E-12080 Castelló, Spain

Delocalized image surface states in free-standing hollow silica nanospheres populated with one or two electrons or an exciton are theoretically predicted for a wide range of internal radii and shell thicknesses. The driving force building up these surface states is the image self-polarization potential originating from the dielectric mismatch between the nanoshell and the surrounding air. The surface states are localized in a spherical crown beyond the nanoshell border. The transition from volume to surface state will then have to overcome the spatial confining potential barrier of the nanoshell. Owing to the different spatial confining barriers of electrons and holes in the silica nanoshell, electron but no hole density can be concentrated in surface distributions. The self-polarization potential looks like a double well potential, each well located just beyond the nanoshell border, with the internal well deeper than the external one, so that an excess carrier is attracted more strongly by the inner interface. This leads the electron density of a surface state to be located mainly in the internal surface of the hollow nanosphere. The shorter the inner nanoshell radius is, the stronger the binding of the excess electron to the surface will be. The volume/surface ground state phase diagrams of the one-electron, two-electron, and exciton systems have been calculated. All three diagrams are quite similar, thus revealing the monoelectronic character of the driving force for the transition from volume to surface states. © *2008 American Institute of Physics.*
[DOI: 10.1063/1.2829802]

I. INTRODUCTION

The colloidal growth of free-standing nanocrystals makes it possible to fabricate the smallest semiconductor nanocrystallites with sizes of just a few nanometers and a spherical shape.[1–5] Wet chemistry methods also allow multi-shell structures built of concentric layers to be synthesized with highly controlled shell thicknesses and compositions.[1–3,6–10] Treating these core-shell composites further (by calcining, chemistry, or photoetching methods) one can finally obtain hollow spheres.[11–13] Hollow spherical materials have aroused a great deal of interest owing to their numerous potential applications in fields such as chromatography, the protection of biologically active agents, fillers, drug delivery, controlled release, adsorption, and catalysis.[14–23] Among these hollow spheres, those made of silica have attracted a lot of attention because of their low cost and feasible synthesis. Both SiO2 micro- and nano-spheres can be obtained with precisely controlled sizes and shell thickness, with the hollow spheres retaining the same size and morphologies as the precursor nanocomposite.[24]

It has been predicted that small free-standing SiO2 nanocrystals can trap electrons in surface states[25] and also that electrons can be trapped in small nanocavities in bulk SiO2;[26] this trapping capability originates from image charges produced by the dielectric mismatch at the SiO2 surface. A key factor for this material to form surface states in nanosized systems is its low electroaffinity[25,26] of only about 0.9 eV.[27] It should be stressed that this trapping capability is not related to the presence of defects as, e.g., surface oxygen vacancies or other morphological features at the surface that have been well characterized as electron trapping sites yielding localized electronic states at the surface of dielectric materials.[28,29]

Despite the extensive potential applications of hollow silica materials, theoretical investigations on their energy structure are rather scarce.[30] In this paper we carry out a theoretical study of the electronic structure of ideal defect-free hollow silica nanospheres in air, for a wide range of the internal radii and thicknesses. We focus on image surface states. One- and two-electron and excitonic states are addressed. As a major result it should be noted that (i) for a large range of radii, image surface ground states are obtained, (ii) electron (negative) density but no hole (positive) density can be concentrated in the hollow nanocrystal surface, and (iii) surface state electron density is basically located in the internal surface. These findings suggest that solid and hollow silica nanospheres will display quite different behaviors when an excess electron comes into them. It should also be noted that, in the case of hollow nanospheres, this excess electron exerts most of its influence on the internal and most active surface of the hollow sphere.

II. THEORY

A. The self-polarization potential

Classical image potentials generated in a neutral solid sphere with radius R and dielectric constant ε_1 in a medium of permittivity ε_2 has the form[31]

$$V_s(r < R) = \frac{1}{\varepsilon_1} \frac{\varepsilon - 1}{2} \sum_{l=0}^{\infty} \frac{l+1}{1 + l(\varepsilon + 1)} \frac{r^{2l}}{R^{2l+1}}, \quad (1)$$

[a]Electronic mail: josep.planelles@qfa.uji.es.

$$V_s(r > R) = -\frac{1}{\varepsilon_2}\frac{\varepsilon - 1}{2}\sum_{l=0}^{\infty}\frac{l}{1 + l(\varepsilon + 1)}\frac{R^{2l+1}}{r^{2l+2}}, \qquad (2)$$

with $\varepsilon = \varepsilon_1/\varepsilon_2$. Its limit of a perfectly conducting sphere in air, $(\varepsilon_1 \to \infty, \varepsilon_2 = 1)$, $V_s(r < R) = 0$, and $V_s(r > R) = -R^3/[2r^2(r^2 - R^2)]$, is well known.[32] This potential decays asymptotically as $-1/r^4$ and thus much faster than the image potential of a planar surface $(-1/4d$, where $d = r - R)$. Consequently, flat surfaces apparently bind electrons in image states more strongly than spheres.

However, this image self-polarization potential diverges as the source charge approaches the dielectric interface, i.e., as $r \to R$. Therefore, the Schrödinger equation including this single-particle potential is found to be nonintegrable, unless we force a null electron density at the interface (e.g., by imposing an impenetrable infinitely high barrier at the sphere border).

This pathological result prompts the question as to whether or not it is sensible to employ classical electrodynamics and the macroscopic parameter defining the dielectric response of the medium when dealing with nanosystems in the framework of a quantum mechanical treatment, as is commonly assumed in the widely employed envelope function approach (EFA).[33] Within this approach, the electron wave function of a nanocrystal is written as a product of smooth envelope functions and Bloch functions, with the Bloch functions having the periodicity of the nanocrystal lattice. The integration of the periodic functions in the Schrödinger equation then yields a set of coupled differential equations for the envelopes. In the case of the one-band model for the conduction electrons, the resulting differential equation for the envelope function is mathematically identical to the Schrödinger equation, in which all integrated details of the unit cell go, on average, into the electron effective mass and the nanocrystal border is reflected in a confining steplike potential with a height amounting to the electroaffinity of the bulk nanocrystal material (or the band offset between neighboring materials if the nanocrystal is buried in a semiconductor matrix). The interaction of conduction band electrons with the rest of electrons and nuclei is averaged as an interaction with a continuous medium capable of being polarized. In other words, EFA retrieves the macroscopiclike view of classical electrodynamics.

The issue of nonintegrability of the Schrödinger equation when self-polarization is included was overcome by Bányai et al.,[31] who proposed a "regularized" self-polarization V_s potential, i.e., a linear interpolation replacing the actual V_s in a thin layer at the interface with thickness of the order of a lattice constant. The underlying assumption is that the electrodynamics of continuous media breaks down in the microscopic domain and that the above mentioned interpolation is a good average. However, this regularized image potential does not have a proper scaling with size. The idea that an appropriate description of V_s requires accounting for the finite thickness of the dielectric interface led to the use of a model in which the steplike dielectric transition is replaced by a smooth continuous variation within a thin layer of the order of a lattice constant located at the nanocrystal interface.[34] This model, which has a proper size scaling,

yields an integrable Schrödinger equation. In the present paper we employ an implementation of this model for numerical calculation in multishell spherical systems reported in Ref. 35.

B. The Hamiltonian

We will focus on one- and two-electron and exciton states of hollow silica nanospheres. The present study has been carried out within the framework of the effective mass and envelope function approximations. Consequently, we employ a macroscopiclike treatment of Coulombic interactions, so that one parameter, the dielectric constant, characterizes the dielectric response of the nanoshell. The corresponding one-electron effective mass Hamiltonian reads (in atomic units, a.u.),

$$H = -\frac{1}{2}\nabla\left[\frac{1}{m^*(\mathbf{r})}\nabla\right] + V(\mathbf{r}) + V_s(\mathbf{r}), \qquad (3)$$

where the first term is the generalized kinetic energy operator accounting for position-dependent effective masses, $V(\mathbf{r})$ represents the spatial confining potential and $V_s(\mathbf{r})$ is the self-polarization potential. When the effective mass approach and the envelope function approximation are used, the confining potential has a well-defined steplike character at interfaces separating two different media, with the rectangular steps being determined in our silica nanoshell by the SiO_2 bulk semiconductor electroaffinity.

The Hamiltonian (a.u.) for two interacting conduction band electrons reads

$$\mathcal{H}(\mathbf{r}_1, \mathbf{r}_2) = \sum_{j=1,2} H_j(\mathbf{r}_j) + V_c(\mathbf{r}_1, \mathbf{r}_2). \qquad (4)$$

$V_c(\mathbf{r}_1, \mathbf{r}_2)$ stands for the generalized Coulomb electron-electron interaction, including dielectric mismatch effects, i.e., including the interaction between each electron and the image charges induced by the others. The explicit expressions for $V_c(\mathbf{r}_1, \mathbf{r}_2)$ are given in Ref. 34. Then, to account for two-electron states we first solve the one-particle eigenvalue equation (3). The radial parts of the exact single-electron eigenfunctions $\phi_{n\ell m}(\mathbf{r})$ are determined numerically on the grid extending far beyond the nanoshell border. Products of the basis functions $\phi_{n\ell m}$ are then used to construct full configuration-interaction (FCI) expansions $\Psi_{LS} = \Sigma_j c_j \Phi_j$ of the symmetry- and spin-adapted two-electron configurations Φ_j, where L and S are the total angular and total spin quantum numbers, respectively. The two-electron Hamiltonian, Eq. (4), is then diagonalized in the FCI basis set. As a result, we get two-particle wave functions $\Psi_{LS}(\mathbf{r}_1, \mathbf{r}_2)$ and energies $E(^{2S+1}L)$. We use a very large orbital basis set $\phi_{n\ell m}$ including the $n = 4$ lowest-lying orbitals with $\ell = 0, 1$, the $n = 3$ lowest-lying orbitals with $\ell = 2 - 5$, and the $n = 2$ lowest-lying orbitals with $\ell = 6 - 8$, with this basis set being large enough to ensure by far the required accuracy.

From the wave function, we can define the *radial density* $\rho(r)$,

$$\rho(r) = 2 \int |\Psi(\mathbf{r},\mathbf{r}')|^2 r^2 r'^2 \sin\theta \sin\theta' \, d\phi d\phi' \, d\theta d\theta' dr' .$$

(5)

Concerning excitons, as we are dealing with the fundamental exciton, which basically involves the fundamental $1S_e$ electron and $1S_{3/2}$ hole states[36,37] and thus has a strong heavy-hole character, we employ the one-band model for the hole, as we have done for the electron. Furthermore, we disregard the electron-hole spin-exchange interaction that splits the optically active exciton ground state into several states,[36,38,39] the lowest of which is optically passive. Thus, the single-particle hole effective mass Schrödinger equation is the same as that for the electron, Eq. (3), but the hole effective mass and confining potential should be inserted in it. Same as above, the radial parts of the exact single-particle eigenfunctions $\phi_{n\ell m}(\mathbf{r}_h)$ are determined numerically on the grid extending far beyond the nanoshell border. Hartree products of the basis functions $\phi_{n\ell m}(\mathbf{r}_e) \cdot \phi_{n'\ell'm'}(\mathbf{r}_h)$ are then used to construct FCI expansions $\Psi_{LM} = \Sigma_j c_j \Phi_j$ of the symmetry-adapted e-h configurations, where L and M are the total and z-component angular quantum numbers, respectively.

The e-h Hamiltonian $\mathcal{H}(\mathbf{r}_e,\mathbf{r}_h) = H_e(\mathbf{r}_e) + H_h(\mathbf{r}_h) + V_c(\mathbf{r}_e,\mathbf{r}_h)$ is then diagonalized in the FCI basis set. As a result, we get two-particle wave functions $\Psi_{LM}(\mathbf{r}_e,\mathbf{r}_h)$ and energies $E(L)$. We employ the same orbital basis set $\phi_{n\ell m}$ as that in the two-electron case (same for electron and hole). It is large enough to ensure by far the required accuracy.

Finally, from the wave function, we define the electron *radial density* $\rho(r_e)$ like in Eq. (5) where now r', θ', ϕ' represent the hole coordinates, and the factor 2 is dropped since now we have just one electron.

We next summarize the parameters employed in our calculations. Electron and hole effective mass and dielectric constant in air have obviously been taken as being unity, while in silica we have $m_e^* = 0.5$, $m_h^* = 10$, electroaffinity $\chi = 0.9$ eV, and dielectric constant $\varepsilon = 4$, see Refs. 27 and 40–43. Since we cannot promote holes in air or a vacuum, we will assume an infinite height for the spatial confining barrier of a hole in the nanoshell. As for electrons, we consider the silica electroaffinity as being the confining barrier height.

C. Computational details

The radial part of the exact single-particle eigenfunctions are determined by solving Eq. (3) numerically in a grid. We discretize this differential equation using central finite differences, following the scheme proposed by Harrison,[44] which ensures the robustness of the method even for large changes in the effective mass across the interfaces. Since a part of the eigenstates are surface states, i.e., are mostly concentrated in a spherical shell about 1 nm thick, a very dense grid is required. We employ 500 points/nm, which is more than capable of rendering the required accuracy. The grid is extended at least 4 nm beyond the external radius of the nanoshell, with the calculations being insensitive to further extension of the grid limit. All calculations employ the same grid. The discretization of Eq. (3) yields eigenvalue problems

of asymmetric, huge, and sparse matrices. Energies and wave functions are obtained by means of diagonalization. To this end we use the Arnoldi solver[45] implemented in the AR-PACK package.[46]

Extensive many-body calculations employing these monolectronic eigenvectors are computationally unfeasible. Hence, out of the above eigenvectors, we built shorter vectors by selecting equally spaced points. We then checked that, using the same many-body basis set, the calculations employing 50, 25, and 10 points/nm yield the same results, within the required accuracy (differences in energy less than 0.1 meV). Therefore, the extensive many-body calculations have been carried out by employing these short single-particle vectors.

III. RESULTS AND DISCUSSION

A. The self-polarization potential

Electrons in image states feel the attractive force of the charge induced in the material even away from the surface, due to the extremely long-ranged Coulomb potential. As discussed in the previous section, the sharp drop in dielectric permittivity between a nanosphere and the surrounding air yields an image potential that is repulsive inside and attractive outside and which may bind carriers in surface states. In accordance with Eq. (2), larger radii R bind more strongly. However, a sharp dielectric drop yields nonintegrable Hamiltonian eigenvalue equations and should be replaced by a continuous variation of the dielectric constant within a lattice-constant range at the sphere border. The resulting $V_s(r)$ profile is continuous, also repulsive inside and attractive outside, with a narrow deep well by the sphere border. In Figs. 1(b) and 1(c) we plot the self-polarization V_s potentials corresponding to two silica nanospheres in air with radii $R = 5$ and 25 nm, respectively. We can see that, as in the case of the sharp model, the attractive part of the potential decays faster as R diminishes. However, as the well depth is finite, this faster decay turns into a deeper well. Additionally, in the region $r < R$, V_s is more repulsive for small values of R. As a result, larger radii R no longer bind more strongly.

In order to conduct a deeper analysis of V_s in Figs. 1(a) and 1(b) we plot the self-polarization V_s potentials of an $R = 5$ nm air bubble in a silica matrix and that of an $R = 5$ nm silica nanocrystal, respectively. The figure is also completed with the self-polarization potential of a hollow silica nanosphere with $R_{in} = 5$ nm and $R_{out} = 25$ nm [Fig. 1(d)]. In Figs. 1(a) and 1(b) we can see that V_s has a plateau in the region $0 < r < R$ that is attractive/repulsive in the air bubble/nanocrystal. Then, $V_s(r=0) \neq 0$ while $V_s(r\to\infty)\to 0$. The hollow sphere self-polarization potential, Fig. 1(d), can be viewed approximately as a superposition of the two kinds of potentials mentioned above [Figs. 1(a) and 1(c)]. As a result, the inner well of this double well potential turns out to be quite a lot more attractive than the external well, so that we can predict that an excess electron will be bound more strongly at the inner interface. Several open questions such as whether the electron density of a surface one-electron state will be distributed in one or both wells, whether or not a second excess electron will be trapped in the same well as
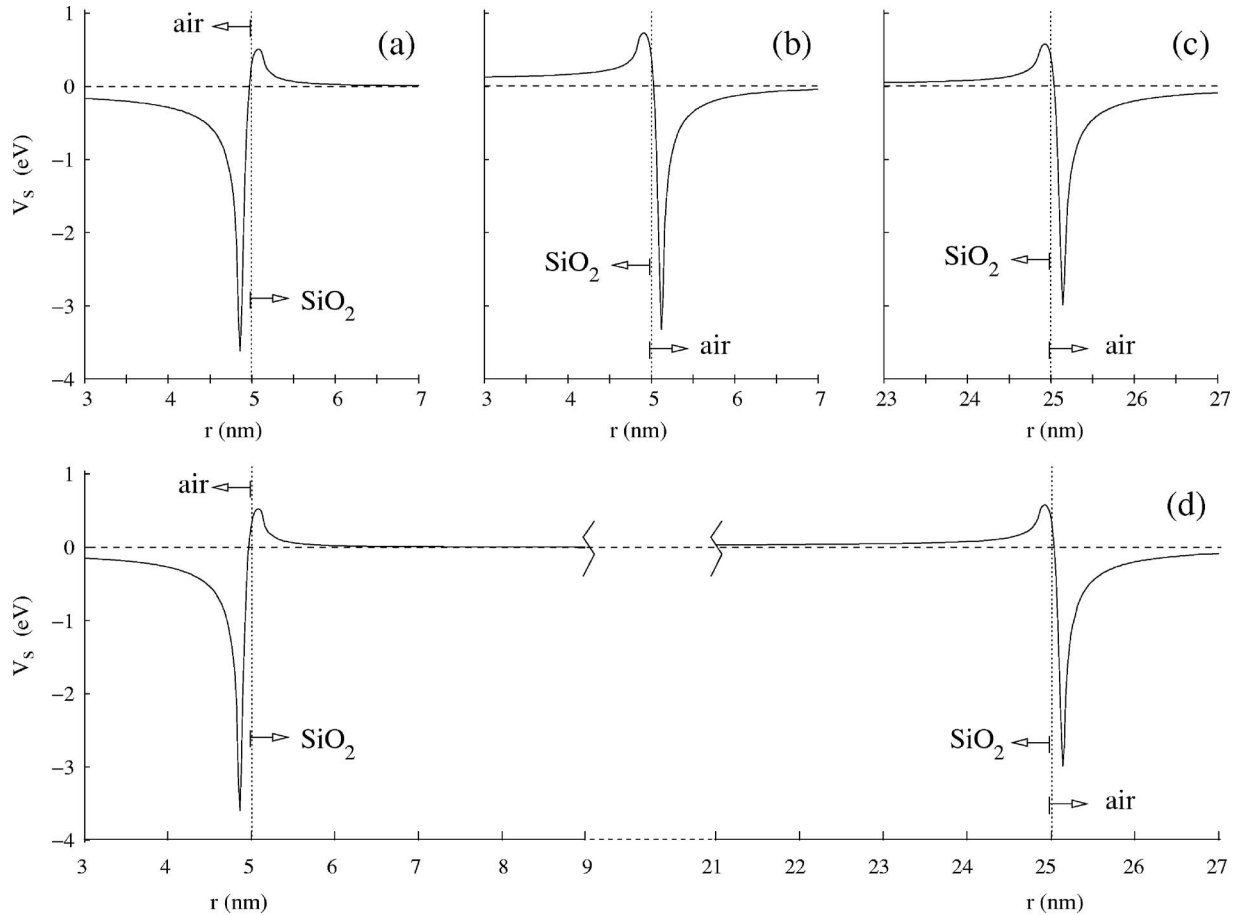
FIG. 1. Self-polarization potential profiles V_s corresponding to (a) an $R=5$ nm air bubble in a silica matrix, (b) an $R=5$ nm silica nanocrystal in air, (c) an $R=25$ nm silica nanocrystal in air, and (d) a hollow silica nanosphere with $R_{in}=5$ nm and $R_{out}=25$ nm.

the first one, and whether the density distribution of the electron and hole of an exciton are influenced to a similar extent by V_s or not will be addressed in the following sections.

B. Image surface states

In order to answer the questions posed at the end of Sec. III A, we have carried out a comprehensive study of single-electron, two-electron, single-hole, and exciton states in silica nanoshells with internal radii R_{in} and shell thicknesses d both ranging from 2 to 28 nm. Many experimentally synthesized silica spherical shells fall within this range.[24,30,47] We deal with single carrier states first in order to investigate the single-particle distribution, which is only determined by the interplay of spatial and self-polarization confining potentials. We will show that in a wide range of geometries the low-lying electron states are surface image states. The extremely high confining potential barrier acting on holes prevents this from being the case for them. As a second electron is introduced in the nanoshell, Coulomb interaction, including the interaction between each electron and the image charges induced by the other one, come into play. We will show that, despite the electron-electron repulsion, the surface ground state ^1S_g only concentrates electronic density in the inner face of the nanoshell. Only some excited two-electron surface states show the electronic density simultaneously distributed in both faces. Finally, we will show that the hole

distribution of the fundamental exciton is always volumetric while, in a large range of geometries, the electron concentrates at the inner interface of the nanoshell.

1. A single carrier in a nanoshell

Here we consider both single-electron and single-hole stationary states. The main difference between electron and hole density distributions in silica nanoshells comes from the different heights of the potential barrier spatially confining either particle. Thus, while it is relatively low for electrons (0.9 eV), it is extremely high for holes. Since the deep self-polarization potential well is located in air, by the nanoshell borders, only electrons can build surface density distributions. We actually find that only the low-lying electron states are surface states. As for the low-lying part of the energy spectra, since the lack of silica in the central core of the nanoshell $(0<r<R_{in})$ energetically favors the radial nodeless orbitals $\phi_{1,\ell m}$, we find that both for electrons and holes and for the entire range of geometries that have been studied, the low-lying states are radial nodeless $\phi_{1,\ell m}$ orbitals. The electron low-lying orbitals with a radial node, particularly the 2s orbital $(\phi_{2,0,0})$, find a source of energetic stabilization in the self-polarization potential wells; this is not the case for holes which are strongly confined within the nanoshell borders. Thus, in the case of the nanoshell that was calculated with the deepest self-polarization potential wells $(R_{in}=d$
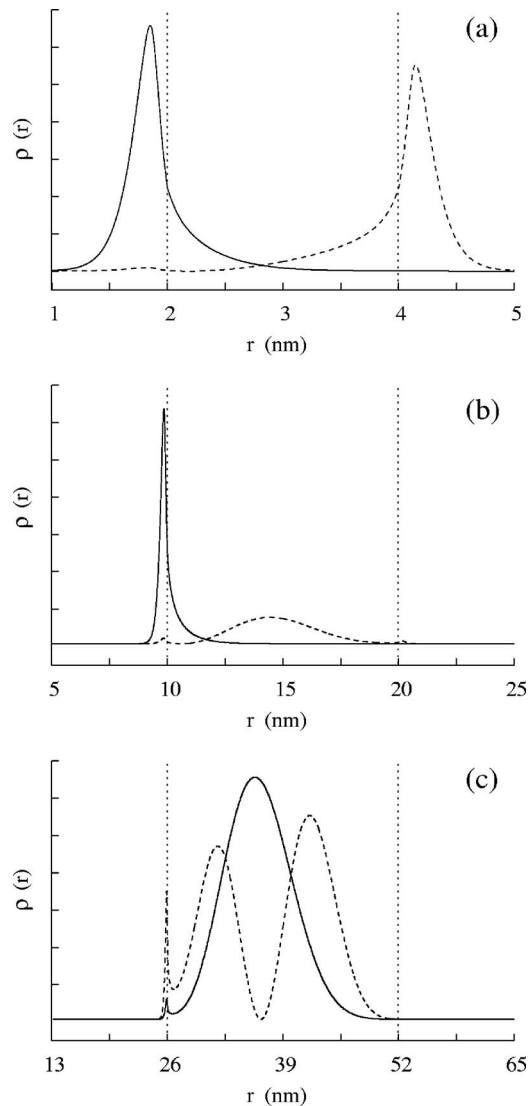
FIG. 2. 1s (full line) and 2s (dashed line) electron radial density distributions in hollow silica nanospheres with an internal radius R_{in} and shell thickness d. (a) $R_{in}=d=2$ nm; (b) $R_{in}=d=10$ nm; and (c) $R_{in}=d=26$ nm. Vertical dotted lines represent the nanoshell borders.

FIG. 3. 1s radial density distributions in hollow silica nanospheres populated with a single electron and dimensions defined by an internal radius $R_{in}=20$ nm and shell thicknesses (a) $d=4$ nm, (b) $d=10$ nm, (c) $d=20$ nm, and (d) $d=28$ nm. Vertical dotted lines represent the nanoshell borders, and ρ_v is the amount of electronic density within the region $(R_{in}+\Delta, R_{in}+d-\Delta)$, where $\Delta=1.5$ Å.

$=2$ nm) the electron orbital sequence is $1s<1p<1d<2s...$, while for holes the $2s$ orbital appears to be energetically less stable than at least the $1k$ orbital ($\phi_{1,8,m}$), with $1k$ being the radial nodeless orbital with the largest ℓ calculated. As R_{in} increases and, consequently, the attractive wells of the self-polarization potential become shallower, this differential behavior between one-radial-node orbitals of electrons and holes vanishes. Thus, for $R_{in}\geqslant 22$ nm, both electron and hole $2s$ orbitals appear energetically more excited than the corresponding $1k$ orbital.

As pointed out above, only electrons can build surface states. Our calculations also reveal that basically only low-lying radial nodeless orbitals can come to the surface and, in such a case, their electronic density is concentrated in the inner nanoshell border. Also, orbitals with a radial node, particularly $2s$, find a source of energetic stabilization in nanoshells with small radius and thickness. As an illustration, in Fig. 2 we plot the electronic radial density distribution of the $1s$ and $2s$ orbitals of three different nanoshells
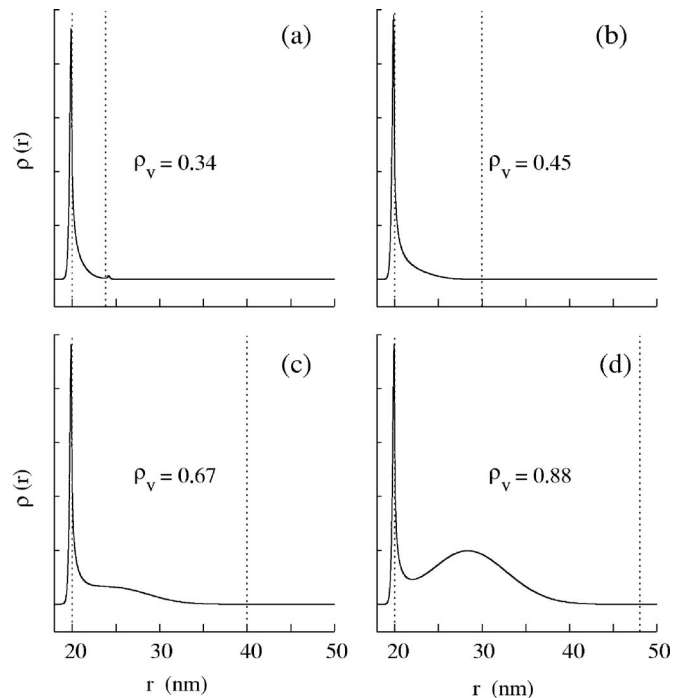
with $R_{in}=d=2$ nm, $R_{in}=d=10$ nm, and $R_{in}=d=26$ nm, respectively. Interestingly, panel 2(a) shows that in the case of the smallest nanoshell ($R_{in}=d=2$ nm) the $1s/2s$ orthogonality promotes the $2s$ electronic density to the external nanoshell surface.

It has been reported[26] that the largest radius of a spherical air bubble in bulk silica that is able to trap electrons in surface states is about 13 nm. Our present calculations reveal that this trapping capability is enhanced in nanoshells. We find that an $R_{in}=20$ nm nanoshell still draws quite a large amount of electronic density at the surface. Figure 3 shows the $1s$ radial density distribution of several nanoshells with $R_{in}=20$ nm and thickness $d=4, 10, 20$, and 28 nm. We see that for $d=10$ nm the nanoshell still has more than 50% of the ground state $1s$ electronic density at the surface, while this is not the case if $d>20$ nm. The phase diagram is drawn in Fig. 4. Below the line (smaller radii and shell thicknesses) the electron builds surface ground states. Since no quantitative definition of surface state can be established, here we have assumed the following criterion. We calculate the amount of electronic density within the region $(R_{in}+\Delta, R_{in}+d-\Delta)$, where $\Delta=1.5$ Å. If it is smaller than 0.3, i.e., 70% of the electronic density is close to the shell border, we define the state as a surface state. The diagram in Fig. 4 shows that surface trapping is larger as both the internal radius and thickness of the shell decrease. Shorter internal radii yield deeper self-polarization potentials, thus producing a larger energetic stabilization of surface states. Shorter shell thicknesses yield stronger confinement, thus energetically destabilizing the volume states to a larger extent. Figure 4 also
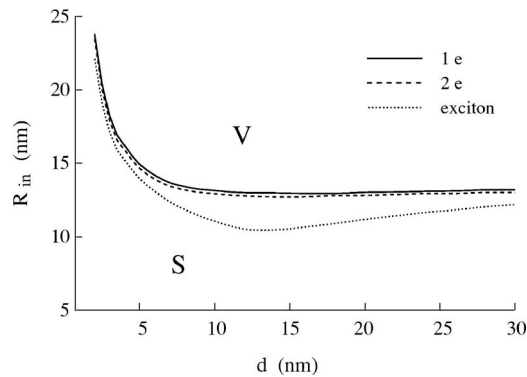
FIG. 4. Electron density phase diagram of hollow silica nanospheres populated with a single electron (full line), an exciton (dotted line), and two electrons (dashed line) vs the internal radius R_{in} and shell thickness d. S/V labels the region where the amount of electronic density close to the shell border is larger/smaller than 70%.
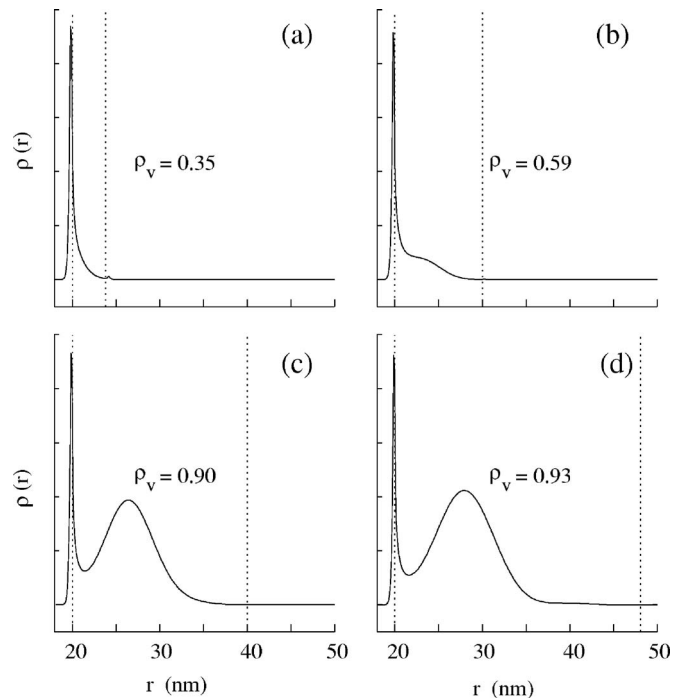

FIG. 5. Electron radial density distribution of the exciton ground state in hollow silica nanospheres with dimensions defined by an internal radius $R_{in}=20$ nm and shell thicknesses (a) $d=4$ nm, (b) $d=10$ nm, (c) $d=20$ nm, and (d) $d=28$ nm. The meanings of vertical dotted lines and ρ_v are the same as in Fig. 3.

reveals that beyond $d=10$ nm the single-electron phase diagram border profile $R_{in}(d)$ does not change by further increasing d, i.e., a further increase in the shell thickness does not produce a relevant energetic stabilization of volume states.

2. Two electrons and excitons in a nanoshell

In this subsection we consider a second particle coming into the nanoshell. If the second excess particle is a hole, we know from previous sections that holes are so highly confined within the nanoshell that they cannot overcome the barrier and draw hole-surface-like distributions over the self-polarization potential well. The (positive) hole distribution of the exciton will therefore be volumetric. If the electron-hole attraction is disregarded, then, for a wide range of nanoshell radii and thicknesses, the (negative) electron distribution forms surface states. We have calculated the phase diagram for the electron distribution of an exciton when the electron-hole interaction is taken fully into account. Our calculations yield a phase diagram for the electron distribution of the fundamental exciton close to that of a single electron in the nanoshell (see Fig. 4). However, while the ground state single-electron phase diagram border profile $R_{in}(d)$ has an exponential-like decay, the corresponding profile for the electron distribution of the ground state exciton shows a shallow minimum at about $d=14$ nm. The phase diagram border profile is now determined by two factors. On the one hand, we have the same single-electron factors yielding an exponential-like decay profile. As pointed out in the previous subsection and as can be seen in Fig. 4, once a shell thickness of about $d=10$ nm is reached, a further increase in d does not change the surface trapping radius $R_{in}(d)$. At this point, the many-body electron-hole attraction becomes relevant. Since the hole distribution is necessarily volumetric, the shorter the shell thickness is, the closer the electron and hole distributions are and the stronger the electron-hole attraction becomes. This many-body effect thus produces an increase in $R_{in}(d)$ vs d. In other words, the trend of the phase diagram border $R_{in}(d)$ profile is determined by single-particle/many-body effects at short/large d values. As a result, a shallow minimum appears in such a profile at about

$d=14$ nm. In Fig. 5 we include the electron density distribution of a set of nanoshells with $R_{in}=20$ nm and shell thicknesses $d=4$, 10, 20, and 28 nm, in order to compare them to their partners in Fig. 3, which correspond to a single electron in the same nanoshells. As a whole, our results reveal that the presence of a (volume-distributed) hole has little influence on the surface electron state density distribution. This evidences, in turn, that the monoelectronic potential image terms prevail over the many-body interactions as a driving force for the transition from volume to surface states, which is partially due to the screening of the bare Coulomb interaction by polarization charges.

We have also calculated the phase diagram for the ground state electron density of two electrons in a nanoshell. One early and surprising result is that we have not found phases in which the electron density is distributed fifty-fifty in volume and surface, or in either nanoshell surface (we found this last phase in some excited states of the two-electron system). The ^1S_g ground state has only two phases. Namely, a phase where all of the density is volumetrically distributed and a second phase in which all of the density is located at the inner nanoshell border forming a surface state; this phase diagram is hardly distinguishable from that of a single electron in the nanoshell (see Fig. 4). In this case, the electron-electron interaction, which is particularly strong, does not promote one of the electrons from the deep self-polarization potential well at the inner nanoshell border to the volume or to the shallow self-polarization potential well at the external border. Both electrons remain at the inner nanosell border but strongly correlated, leading to an angular Wigner-like distribution.[48] In other words, although the elec-
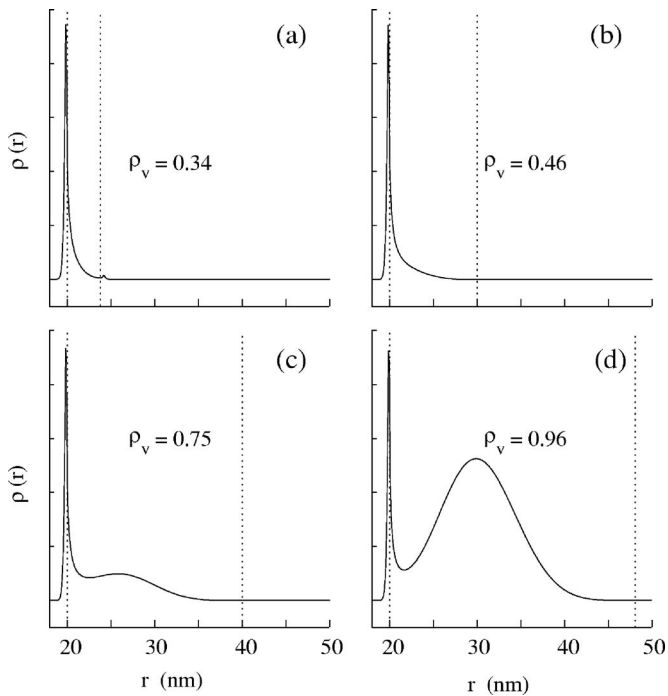
FIG. 6. Electron radial density distribution of the two-electron ground state in hollow silica nanospheres with dimensions defined by an internal radius $R_{in}=20$ nm and shell thicknesses (a) $d=4$ nm, (b) $d=10$ nm, (c) $d=20$ nm, and (d) $d=28$ nm. The meanings of vertical dotted lines and ρ_v are the same as in Fig. 3.

tron density distribution is strongly modified as the second electron comes into play, no relevant amount of electronic density is promoted into the nanoshell volume. The strongly correlated two-electron surface state has the electron density located over the deep self-polarization potential well at the inner nanoshell border in diametrically opposite sites. For the sake of completeness, in Fig. 6 we enclose the radial density distribution $\rho(r)$ of the ^1S_g two-electron ground state of a nanoshell with an internal radius $R_{in}=20$ nm and several shell thicknesses $d=4$, 10, 20, and 28 nm, in order to compare them with Figs. 3 and 5, which show the electron density distribution of a single electron and an exciton in the same nanoshells.

IV. CONCLUDING REMARKS

We have calculated single-particle, two-electron, and exciton states of free-standing silica nanoshells for a wide range of internal radii and thicknesses. We have found that the sharp dielectric drop at the nanoshell border can lead to the formation of delocalized surface states. In such a case, only electronic density but not hole density come to the (internal) surface of the nanoshell. The phase diagrams of one-electron, two-electron, and exciton ground states have been calculated. All three diagrams are quite similar, i.e., the second excess (positive or negative) particle has little effect on the position of the border separating volumetric and surface states in the phase diagram, which reveals the monoelectronic character of the driving force for the transition from volume to surface states.

[1]A. Mews, A. Eychmüller, M. Giersig, D. Schoos, and H. Weller, J. Phys. Chem. **98**, 934 (1994).
[2]A. P. Alivistatos, Nature (London) **271**, 933 (1996).
[3]A. Mews, A. V. Kadavanich, U. Banin, and A. P. Alivisatos, Phys. Rev. B **53**, R13242 (1996).
[4]D. Norris and M. G. Bawendi, Phys. Rev. B **53**, 16338 (1996).
[5]R. B. Little, M. A. El-Sayed, G. W. Bryant, and S. Burke, J. Chem. Phys. **114**, 1813 (2001).
[6]C. A. Mirkin, R. L. Letsinger, R. C. Mucic, and J. J. Storhoff, Nature (London) **382**, 607 (1996).
[7]U. Banin, Y. Cao, D. Katz, and O. Millo, Nature (London) **400**, 542 (1999).
[8]Y. Cao and U. Banin, J. Am. Chem. Soc. **122**, 9692 (2000).
[9]O. Millo, D. Katz, Y. Cao, and U. Banin, Phys. Rev. Lett. **86**, 5751 (2001).
[10]M. Braun, C. Burda, and M. A. El-Sayed, J. Phys. Chem. A **105**, 5548 (2001).
[11]M. Giersig, T. Ung, L. M. Liz-Marzan, and P. Mulvaney, Adv. Mater. (Weinheim, Ger.) **9**, 570 (1997).
[12]F. Caruso, Adv. Mater. (Weinheim, Ger.) **13**, 11 (2001).
[13]T. Tirimoto, J. P. Reyes, K. Iwasaki, B. Pal, T. Shibayama, K. Sugawara, H. Takahashi, and B. Ohtani, J. Am. Chem. Soc. **126**, 316 (2003).
[14]S. Schacht, Q. Huo, I. G. Voigt-Martin, G. D. Stucky, and F. Schüth, Science **273**, 768 (1996).
[15]F. Caruso, R. A. Caruso, and H. Mohwald, Science **282**, 1111 (1998).
[16]P. Jiang, J. F. Bertone, and V. L. Colvin, Science **291**, 453 (2001).
[17]S. W. Kim, M. Kim, W. Y. Lee, and T. Hyeon, J. Am. Chem. Soc. **124**, 7642 (2002).
[18]W. Li, X. Sha, W. Dong, and Z. Wang, Chem. Commun. (Cambridge) **2002**, 2434.
[19]Y. Li, J. Shi, Z. Hua, H. Chen, M. Ruan, and D. Yan, Nano Lett. **3**, 609 (2003).
[20]X. Xu and S. A. Asher, J. Am. Chem. Soc. **126**, 7940 (2004).
[21]J. F. Chen, H. M. Ding, J. X. Wang, and L. Shao, Biomaterials **25**, 723 (2004).
[22]Y. Wang, L. Cai, and Y. Xia, Adv. Mater. (Weinheim, Ger.) **17**, 473 (2005).
[23]Y. Zhu, J. Shi, W. Shen, X. Dong, J. Feng, M. Ruan, and Y. Li, Angew. Chem., Int. Ed. **44**, 5083 (2005).
[24]F. Teng, Z. Tian, G. Xiong, and Z. Xu, Catal. Today **93–95**, 651 (2004).
[25]J. L. Movilla, J. Planelles, and W. Jaskólski, Phys. Rev. B **73**, 035305 (2006).
[26]J. Planelles and J. L. Movilla, Phys. Rev. B **73**, 235350 (2006).
[27]J. Robertson, J. Vac. Sci. Technol. B **18**, 1785 (2000).
[28]M. Chiesa, M. C. Paganini, E. Giamello, D. M. Murphy, C. Di Valentin, and G. Pacchioni, Acc. Chem. Res. **39**, 861 (2006).
[29]E. B. Bussmann, N. Zheng, and C. C. Williams, Nano Lett. **6**, 2577 (2006).
[30]Y. Le, M. Pu, and J.-F. Chen, Mater. Res. Bull. **41**, 1714 (2006).
[31]L. Bányai, P. Gilliot, Y. Z. Huand, and S. W. Koch, Phys. Rev. B **45**, 14136 (1992).
[32]J. D. Jackson, *Classical Electrodynamics* (Wiley, New York, 1962).
[33]G. Bastard, *Wave Mechanics Applied to Semiconductor Heterostructures* (Les Éditions de Physique, Les Ulis, 1988); J. P. Loehr, *Physics of Strained Quantum Well Lasers* (Kluwer, Boston, 1998).
[34]P. G. Bolcatto and C. R. Proetto, J. Phys.: Condens. Matter **13**, 319 (2001); this model was previously employed in the case of quantum wells, see F. Stern, Phys. Rev. B **17**, 5009 (1978).
[35]J. L. Movilla and J. Planelles, Comput. Phys. Commun. **170**, 144 (2005).
[36]A. D. Yoffe, *Advances in Physics* (Taylor & Francis, London, 2001), Vol. 50.
[37]V. A. Fonoberov, E. P. Pokatilov, and A. A. Balandin, Phys. Rev. B **66**, 085310 (2002).
[38]F. A. Reboredo and A. Zunger, Phys. Rev. B **63**, 235314 (2001); A. Franceschetti, L. W. Wang, H. Fu, and A. Zunger, *ibid.* **58**, R13367 (1998).
[39]K. Leung and K. B. Whaley, Phys. Rev. B **56**, 7455 (1997).
[40]Z. A. Weinberg, J. Appl. Phys. **53**, 5052 (1982).

[41]F. Gustini, P. Umari, and P. Pasquarello, Microelectron. Eng. **72**, 299 (2004).

[42]J. M. Ferreyra and C. R. Proetto, Phys. Rev. B **52**, R2309 (1995).

[43]E. F. da Silva, Jr., E. A. de Vasconcelos, B. D. Stosić, J. S. de Sousa, G. A. Farias, and V. N. Freire, Mater. Sci. Eng., B **74**, 188 (2000).

[44]P. Harrison, *Quantum Wells, Wires and Dots* (Wiley, Chichester, 2001), p. 88.

[45]W. E. Arnoldi, Q. Appl. Math. **9**, 17 (1951); Y. Saad, *Numerical Methods for Large Scale Eigenvalue Problems* (Halsted, New York, 1992); R. B. Morgan, Math. Comput. **65**, 1213 (1996).

[46]R. B. Lehoucq, K. Maschhoff, D. C. Sorensen, P. A. Vu, and C. Yang, *ARPACK*: FORTRAN *subroutines for solving large scale eigenvalue problems* (Release 2.1, available at http://www.caam.rice.edu/software/ ARPACK); R. B. Lehoucq, D. C. Sorensen, and C. Yang, *ARPACK User's Guide: Solution of Large-Scale Eigenvalue Problems with Implicit Restarted Arnoldi Methods* (SIAM, Philadelphia, 1998).

[47]Y. Le, J.-F. Chen, J.-X. Wang, L. Shao, and W.-Ch. Wang, Mater. Lett. **58**, 2105 (2004); J.-F. Chen, J.-X. Wang, R.-J. Liu, L. Shao, and L.-X. Wen, Inorg. Chem. Commun. **7**, 447 (2004); J.-F. Chen, Y.-H. Wang, F. Guo, X.-M. Wang, and Ch. Zheng, Ind. Eng. Chem. Res. **39**, 948 (2000).

[48]The formation of a Wigner-like distribution is revealed by calculations carried out (not shown) of the angular correlation density $Z(\theta)$ $=N_Z|\Psi((r_{max},0,0),(r_{max},\theta,0))|^2$, where r_{max} corresponds to the coordinate r of the $\rho(r)$ maximum and N_Z represents the appropriate normalization factor. See also Refs. 25 and 49.

[49]J. L. Movilla and J. Planelles, Phys. Rev. B **74**, 125322 (2006).